Ultramicroscopy 255 (2024) 113861

Contents lists available at ScienceDirect

Ultramicroscopy

journal homepage: www.elsevier.com/locate/ultramic

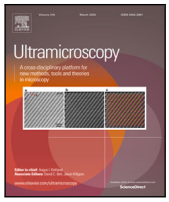

Scanning precession electron diffraction data analysis approaches for phase mapping of precipitates in aluminium alloys

E. Thronsen [a,b,*], T. Bergh [a,c], T.I. Thorsen [a], E.F. Christiansen [a], J. Frafjord [a], P. Crout [d], A.T.J. van Helvoort [a], P.A. Midgley [d], R. Holmestad [a]

[a] Department of Physics, Norwegian University of Science and Technology (NTNU), N-7491 Trondheim, Norway
[b] Materials and Nanotechnology, SINTEF Industry, N-7465, Trondheim, Norway
[c] Department of Chemical Engineering, NTNU, N-7491 Trondheim, Norway
[d] Department of Materials Science and Metallurgy, University of Cambridge, CB3 0FS Cambridge, UK

ARTICLE INFO

Dataset link: https://doi.org/10.5281/zenodo.6645396, https://github.com/elisathr/SPED-phase-mapping/tree/main

Keywords:
Electron crystallography
Transmission electron microscopy (TEM)
Phase mapping
4D-STEM
Scanning precession electron diffraction

ABSTRACT

Mapping the spatial distribution of crystal phases with nm-scale spatial resolution is an important characterisation task in studies of multi-phase materials. One popular approach is to use scanning precession electron diffraction which enables semi-automatic phase mapping at the nanoscale by collecting a single precession electron diffraction pattern at every probe position over regions spanning up to a few micrometers. For a successful phase mapping each diffraction pattern must be correctly identified. In this work four different approaches for phase mapping of embedded precipitates in an Al-Cu-Li alloy are compared on a sample containing three distinct crystal phases. These approaches are based on: non-negative matrix factorisation, vector matching, template matching and artificial neural networks. To evaluate the success of each approach a ground truth phase map was manually created from virtual images based on characteristic phase morphologies and compared with the deduced phase maps. The percentage accuracy of all methods when compared to the ground truth was satisfactory, with all approaches obtaining scores above 98%. The optimal method depends on the specific task at hand. Non-negative matrix factorisation is suitable with limited prior data knowledge but performs best with few unique diffraction patterns and requires substantial post-processing. It has the advantage of reducing the dimensionality of the dataset and handles weak diffracted intensities well given that they occur repeatedly. The current vector matching implementation is fast, simple, based only on the Bragg spot geometry and requires few parameters. It does however demand that each Bragg spot is accurately detected in each pattern and the current implementation is limited to zone axis patterns. Template matching handles a large range of orientations, including off-axis patterns. However, achieving successful and reliable results often require thorough data pre-processing and do require adequate diffraction simulations. For artificial neural networks a substantial setup effort is demanded but once trained it excels for routine tasks, offering fast predictions. The implemented codes and the data used are available open-source. These resources and the detailed assessment of the methods will allow others to make informed decisions when selecting a data analysis approach for 4D-STEM phase mapping tasks on other material systems.

1. Introduction

Materials science abounds with examples of multi-phase materials whose properties are affected by the presence and distribution of various crystal phases. Fast and reliable crystal phase mapping wherein each pixel in a real-space image is assigned to its respective phase is an invaluable tool in understanding and improving such materials. Often, phase mapping with nanometre-scale spatial resolution is required, for example when working with alloys containing embedded nanoscale precipitates [1], interfacial layers at dissimilar metal joints [2] or additively manufactured components [3]. This paper will focus on heat-treatable aluminium (Al) alloys which typically exhibit a distribution of nanoscale precipitates embedded in the Al face-centred cubic (fcc) matrix [1]. Here the precipitate distribution depends strongly on the Al alloy composition and thermomechanical treatment, and quantification in terms of phase and volume fraction is crucial for improved understanding and alloy design.

(Scanning) transmission electron microscopy ((S)TEM) is a powerful characterisation tool for studying nanoscale structures exhibiting

* Corresponding author at: Materials and Nanotechnology, SINTEF Industry, N-7465, Trondheim, Norway.
E-mail address: Elisabeth.thronsen@sintef.no (E. Thronsen).

https://doi.org/10.1016/j.ultramic.2023.113861
Received 12 July 2023; Received in revised form 22 September 2023; Accepted 27 September 2023
Available online 6 October 2023

a suitable spatial resolution alongside an ability to record a range of signals simultaneously. One sub-approach within the field is four-dimensional (4D)-STEM, in which a two-dimensional (2D) diffraction pattern is recorded for each probe position within a 2D real space raster [4,5]. 4D-STEM can be performed at a range of convergence angles, with the low convergence semi-angle (~1 mrad) regime typically being referred to as either scanning nanobeam diffraction or scanning electron diffraction [6]. To improve the data quality from a 4D-STEM experiment it can be advantageous to include precession [7]. This defines an experimental scheme known as scanning precession electron diffraction (SPED) [7–9]. Precession electron diffraction (PED) involves tilting the incident beam at an angle from the optical axis (the precession angle) before 'rocking' through a range of azimuthal tilts (most commonly the full hollow cone) [7,8]. After these beams have passed through the sample they are 'de-rocked' by an opposite beam precession. This creates a pattern that can be qualitatively similar to those predicted by kinematical diffraction. A key benefit of using SPED in a phase mapping setting is that the integration (in reciprocal space) leads to more spots and an increased uniformity within Bragg disks by reducing the significance of dynamical diffraction effects. This approach has gained recognition as a robust technique for both phase and orientation mapping [10].

4D-scanning transmission electron microscopy (STEM)-based phase and orientation mapping continues to gain popularity, supported by the introduction of the new direct electron detectors and an ever increasing computational power. Several studies have reported significant improvement in the reliability of phase mapping results when using direct electron detectors as opposed to the conventional approach of using an external digital camera filming the fluorescent screen [11,12]. However the improved detector technology leads to a substantial increase in data size, meaning that data analysis methods need to be further developed.

The default route for orientation and/or phase mapping has been the template matching approach introduced by Rauch et al. [10,13], which involves creating a library of simulated kinematic diffraction patterns for all candidate phases and orientations. The experimental patterns are then compared to the library via a normalised cross-correlation to find the best match. This well-established method has seen extensive usage since its inception with excellent studies produced for both phase [14–17] and orientation mapping [9,12,14,16,18]. The approach is not without limitations though. Results can depend strongly on the correct candidate phase, correct simulation parameters and the pre-processing regime chosen.

Another option when candidate phases (and orientations) are known is to first detect the Bragg peaks in each recorded pattern before then evaluating their geometry. This approach shares many features with the strategies used in the structure solution community. A number of variation exist within the literature; many approaches compare the experimental vectors to reference vectors calculated from crystal structures that are known using electron diffraction [19–21] or X-rays [22], some determine a 2D lattice [23] and others have gone so far as to determining the lattice parameters 'on the fly' [24]. Although they show promise, such approaches have not gained momentum in the S(P)ED community compared to the template matching approach [25]. In the current work, the implemented vector-based approach will be referred to as 'vector matching'.

Due to the vastness of the data produced by S(P)ED experiments it is also reasonable to consider modern 'big data' approaches for some tasks [26,27], as opposed to 'rule-based' approaches such as vector matching and template matching. The use of machine learning approaches to analyse electron microscopy data is increasing, examples include determining the thickness and tilt of the sample [28], high throughput electron backscatter diffraction [29] and other examples as seen in the recent review article by Botifoll et al. [27]. In this work, one approach from each of the two primary branches of modern machine learning, i.e. supervised and unsupervised learning [30], are presented.

Table 1
The nominal composition of the studied Al-Cu-Li alloy.

	Cu	Li	Mn	Fe
wt.%	3.00	1.50	0.55	0.20

NMF is an unsupervised machine learning technique similar to the prevalent principal component analysis (PCA) approach. Unlike PCA, NMF requires the user to specify how many components to retain [31]. The components and weights are also constrained to be non-negative, and may be linearly combined to recreate the majority of the dataset. For SPED data, the component patterns resemble diffraction patterns while the weights resemble diffraction contrast images. NMF has proven to be useful in SPED data analysis as it allows dimensionality reduction and can handle overlap of crystals along the viewing direction [9,32–36]. Furthermore, NMF has proved valuable in phase mapping of precipitates in Al-Mg-Si(-Cu) alloys [37–41]. It is worth noting that NMF itself does not produce phase maps directly. Instead the components must be labelled and post-processed, which is typically a manual process. This fact, coupled with the crucial need to determine a suitable number of components and initialisation means that NMF is not a 'simple and straight-forward' solution for a general phase mapping task.

In contrast to unsupervised learning, supervised learning requires labelled training data, and the success (or failure) of many attempts hinges on the quality of the training data provided. In 4D-STEM, the training data can be simulated data [28]. Kinematical simulations are easier to set up and slightly more resilient to incorrect sample parameters. However this comes at the cost of discarding possibly important physical effects caused by dynamical diffraction, e.g. thickness and small orientation variation affecting intensity distributions. In this work, an ANN is used as the supervised approach. This was chosen since ANNs have been used previously to study 4D-STEM data [28,42] and are well suited for image classification tasks.

In this work, these four approaches for assigning phases to pixels from a SPED scan taken of a standard field-emission gun TEM are compared in terms of both accuracy and user dependency of the resulting phase map. This study used a demonstration dataset acquired from a sample of an Al-Cu-Li alloy that contains two precipitate phases that exhibit known orientation relationships with the Al matrix [43]. This is an ideal model case since the phases can be identified based on morphology, hence and independent verification of the deduced phase maps is possible. The goal of this work is to provide insight into and guidance on how to conducting phase mapping with SPED.

2. Material and data collection

2.1. Material

The model system chosen for this work was an Al-Cu-Li alloy supplied by American Elements with a nominal composition shown in Table 1. The alloy was homogenised for 4 h at 400 °C, extruded as a bar with a diameter of 20 mm, and cut into 13 mm long sections. The sections were solution heat treated for 1 h at 400 °C, water quenched, naturally aged for 10 min at room temperature, and finally artificially aged for 24 h at 250 °C.

The thermomechanical processing produced two distinct, co-existing precipitate phases, namely the hexagonal T_1-Al_2CuLi and the tetragonal θ'-Al_2Cu phase. The space group, lattice parameters and atomic positions for the phases Al [44], T_1 [45] and θ' [46] are shown in Table 2. T_1 precipitates form as plates on $\{111\}_{Al}$ planes and have the following orientation relationship with the Al fcc lattice [47]:

$$(001)_{T_1} \,//\, (111)_{Al}, \langle 110\rangle_{T_1} \,//\, \langle 112\rangle_{Al}. \quad (1)$$

Table 2
Space groups, lattice parameters and atomic positions for the phases Al [44], T_1 [45] and θ′ [46]. The atomic positions are given as fractional coordinates. Note that the unit cell for T_1 was compressed as compared to Ref. [45] to match with $a_{Al} = 4.04$ Å.

Phase	Space group	Lattice parameters [Å]	Atomic positions			Atom
			x	y	z	
Al	$Fm\bar{3}m$ (No. 225)	$a = 4.04$	0.00	0.00	0.00	Al
			0.00	0.50	0.50	Al
			0.50	0.00	0.50	Al
			0.50	0.50	0.00	Al
T_1	P6/mmm (No.191)	$a = 4.95$, $b = 14.15$	1/3	0.00	0.00	Al
			0.00	0.50	0.406	Al
			2/3	1/3	0.161	Cu
			1/2	0.00	0.324	Cu
			0.00	0.00	0.199	Li
			1/3	2/3	0.500	Li
θ′	$I\bar{4}m2$ (No. 119)	$a = 4.04$, $c = 5.80$	0.00	0.00	0.00	Al
			0.00	0.00	0.50	Al
			0.00	0.50	0.25	Cu

θ′ precipitates form as plates on $\{001\}_{Al}$ planes and exhibit the following orientation relationship [43]:

$$(001)_{\theta'} \,//\, (001)_{Al}, \langle 100\rangle_{\theta'} \,//\, \langle 100\rangle_{Al}. \quad (2)$$

The T_1 and θ′ precipitates show different morphologies when viewed in projection along the $\langle 001\rangle_{Al}$ zone axis and can therefore be distinguished based on their shapes in BF or dark-field (DF) images [45,46]. In this work, all transmission electron microscopy (TEM) data was collected with the incident beam at the $\langle 001\rangle_{Al}$ zone axis. Following the orientation relationship in Eq. (1), T_1 precipitates were viewed along zone axis $\langle 0\bar{4}1\rangle_{T_1}$, with two possible orientations along the $\langle 001\rangle_{Al}$ axis. The θ′ precipitates with the orientation relationship in Eq. (2), were viewed along the $\langle 001\rangle_{\theta'}$ and $\langle 100\rangle_{\theta'}$ zone axes, denoted $\theta'_{[001]}$ (viewed face on) and $\theta'_{\langle 100\rangle}$ (viewed edge on), respectively. There is only one unique in-plane rotation angle for $\theta'_{[001]}$, while two perpendicular in-plane rotation angles are possible for $\theta'_{\langle 100\rangle}$. In total, six unique diffraction patterns were expected to appear in the SPED data: one from Al, one from $\theta'_{[001]}$, two from $\theta'_{\langle 100\rangle}$ and two from T_1.

TEM specimens were prepared by mechanical grinding of sections down to ~100 μm thickness and punching them into 3 mm disks. The disks were subsequently electropolished using an electrolyte mixture of 1/3 HNO_3 and 2/3 CH_3OH with a Struers TenuPol-5 machine. The electrolyte was kept at 25 ± 5 °C and the applied voltage was 20 V.

2.2. Scanning precession electron diffraction

TEM was performed on a JEOL JEM-2100F operated at 200 kV. For SPED, the microscope was operated in nanobeam diffraction (NBD) mode, and the precession of the probe was aligned according to the approach described in Ref. [48] using the NanoMEGAS P1000 scan generator and DigiSTAR control software. The convergence semi-angle was 1.13 ± 0.09 mrad, the precession angle 1.04 ± 0.05 ° (18.1 ± 0.9 mrad) and the precession frequency 100 Hz. The SPED datasets were recorded on a Medipix3 MerlinEM direct electron detector from Quantum Detectors [49] with 256 × 256 pixels. The PED patterns were recorded in 2 × 12-bit mode with an exposure time per pattern of 10 ms. The nominal probe size was set to 1.3 nm. The scan step size was chosen to be 4.6 nm. A dataset, termed 'Dataset A' containing 512 × 512 scan pixels was used for the analysis, corresponding to an area of approximately 2.4 μm^2. The second dataset, 'Dataset B', was acquired to verify the robustness of the approaches on other datasets from the same material system. The parameters were the same as above, except that the scan step size was set to 2.3 nm. Results from Dataset A is presented in the main text, while the results from Dataset B are shown in Section S1 in the supplementary material.

3. Algorithms and implementations

3.1. Pre-processing

The raw data was pre-processed using the open-source python library *pyxem* [50]. The patterns were first centred with respect to the direct beam to correct for tilt-shift purity. The direct beam position in each pattern was found by calculating using a centre of mass (COM) approach. After centering, reciprocal lengths were calibrated using the Al {400} reflections of the dataset mean diffraction pattern. The patterns were binned to 128 × 128 pixels before being normalised with respect to the maximum intensity in each pattern. The pre-processing is schematically shown in Fig. 1.

For both the template matching and the ANN approach patterns were subjected to a $\log_{10}$ transform given as:

$$I[k_{x_i}, k_{y_i}] = \log(I_0[x_i, y_i] + a) - \log(a), \quad (3)$$

where $I_0[x_i, y_i]$ is the intensity in pixel (x_i, y_i) and a is a small constant shift which is added to account for pixels with zero intensity. The value of a was chosen to optimise the phase maps by calculating the accuracies for a range of a values in both cases.

3.2. Ground truth phase map creation

A ground truth phase map was created based on manual assignment of VDF images by a cohort of the authors. The construction of the ground truth is presented in Section S2 in the supplementary material. As phases in different orientations have different diffraction patterns, the two distinct orientation of the θ′ precipitates ($\theta'_{[001]}$ and $\theta'_{\langle 100\rangle}$) were assigned to different categories. Thus the 'phase maps' include the categories Al, T_1, $\theta'_{[001]}$ and $\theta'_{\langle 100\rangle}$ as well as a fifth category for unlabelled pixels termed 'not indexed'. In some regions of the sample precipitates overlapped along the beam path. In such cases, the pixel was assigned to a single phase with the following priorities: (1): $\theta'_{\langle 100\rangle}$, (2): T_1 and (3): $\theta'_{[001]}$. This prioritisation scheme was chosen since $\theta'_{\langle 100\rangle}$ tended to give the most intense Bragg spots and $\theta'_{[001]}$ the weakest. The accuracy of the final phase maps were determined by taking the pixel-by-pixel difference between the ground truth phase map and the calculated phase map and finding the percentage of non-zero pixels. This is equivalent to a simple binary scoring process.

3.3. Electron diffraction simulations

The vector matching, template matching and ANN methods all require diffraction simulations of some form to be provided as inputs. The simulations were produced by the open-source python library *diffsims* [51]. These simulations are based on kinematical diffraction theory [52]. For precessed data, it is important to consider the parameter referred to as 'maximum excitation error', $\max\{s\}$. If the excitation error of a reciprocal lattice vector exceeded $\max\{s\}$ the intensity of its corresponding Bragg spot was set to zero. $\max\{s\}$ has a large influence on the number of Bragg spots included in the simulations and the relative intensities.

The calibrations obtained from the experimental data were used in all simulations and the simulated patterns were 128 × 128 pixels. To simulate zone axis patterns for each of the phases the orientation relationships given in Eqs. (1) and (2) were used. The azimuthal angle, ϕ_A, was defined as the in-plane rotation angle. The following Euler angles in the 'zxz' Bunge convention were used: (ϕ_A, 0.0, 0.0) for Al, (ϕ_A, 54.7, 45.0) and (ϕ_A±45.0, 54.7, 60.0) for T_1, (ϕ_A, 90.0, 0.0) and (ϕ_A+90.0, 90.0, 0.) for $\theta'_{\langle 100\rangle}$, and ($\phi_A$, 0., 0.) for $\theta'_{[001]}$. The crystal structures and corresponding simulated zone axis patterns are shown in Fig. 2. The shown simulated patterns were prepared using $\max\{s\}$ equal to 0.030 $Å^{-1}$, 0.050 $Å^{-1}$, 0.030 $Å^{-1}$ and 0.022 $Å^{-1}$ for Al, $\theta'_{[001]}$, $\theta'_{\langle 100\rangle}$ and T_1, respectively.

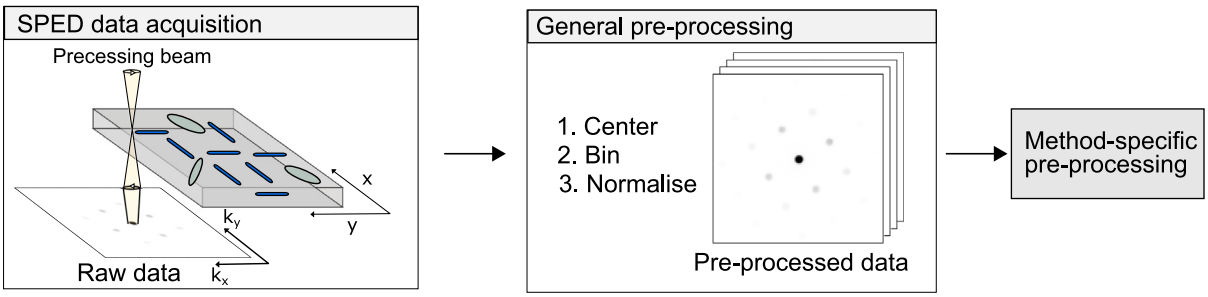

Fig. 1. Schematic illustration of the SPED data acquisition and pre-processing routines. The pre-processing steps that were common for all phase mapping approaches are: centering of the direct beam, binning and normalisation. Certain approaches relied on further pre-processing steps, as explained in the following sections.

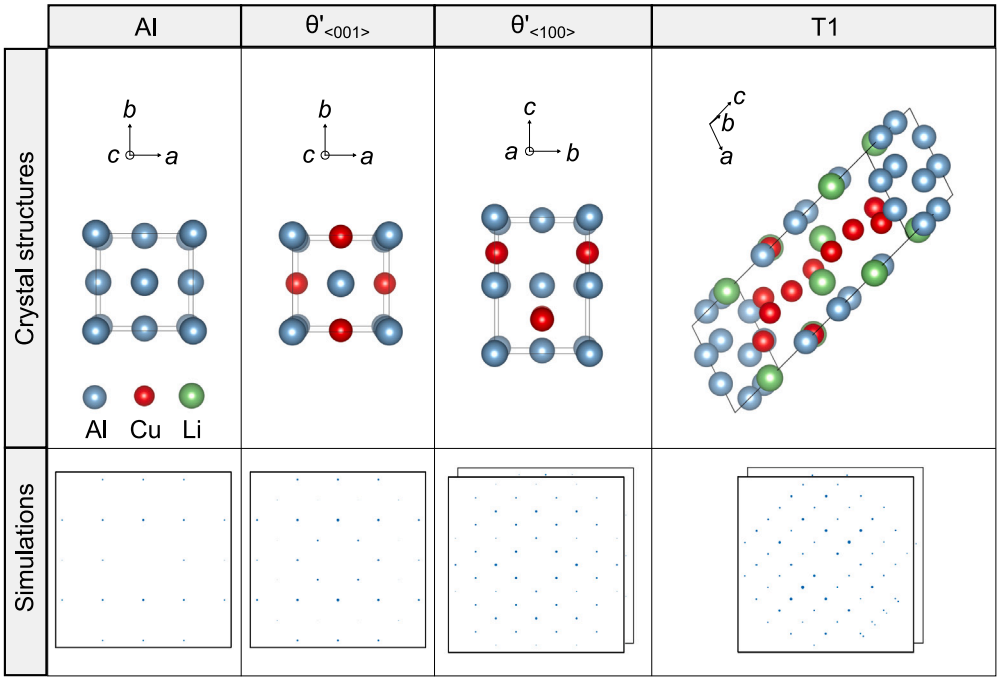

Fig. 2. Illustrations of the crystal structures and corresponding kinematical diffraction simulations for Al viewed along zone axis $\langle 001\rangle_{Al}$, θ′ along $\langle 001\rangle_{\theta'}$ and $\langle 100\rangle_{\theta'}$ and T_1 along $\langle 0\bar{4}1\rangle_{T_1}$. The crystal structures were visualised using the crystallographic software VESTA [53]. In the simulated patterns, Bragg spots displayed with larger radii are more intense.

3.4. Non-negative matrix factorisation

The first step in the approach based on NMF was to exclude certain regions in reciprocal space that were not phase discriminative. Since the precipitate Bragg reflections are the most important for phase mapping, the direct beam, high scattering angles, and the matrix Bragg reflections were masked out. This was done by applying an inner (0.1595 $Å^{-1}$) and an outer (0.7001 $Å^{-1}$) cut-off radius and then creating circular masks centred on the Bragg reflections from the Al matrix as identified by Laplacian of Gaussian peak finding in the average diffraction pattern.

Subsequently, NMF was performed using the scikit-learn implementation [54] included in *hyperspy* [55]. NMF was initialised using the non-negative double singular value decomposition (NNDSVD) initialisation [56]. In order to obtain meaningful results from NMF (i.e. results where the output factors resemble physical diffraction patterns and the loadings resemble diffraction contrast images) it is important that a suitable value is chosen for the number of components, n [32,34,57,58]. To make this choice, singular value decomposition (SVD) was performed to get an indication of a reasonable starting point for n [32]. However, the actual decision on the best value of n must be made by manual inspection in each case. In this approach, we use trial-and-error to find the lowest value of n that produced a one-to-one component-phase result. The NMF components were manually classified based on their similarity to simulated precipitate PED patterns, and the loading maps were then assigned to one precipitate phase category and thresholded to form binary phase maps.

Not all of the phases could be properly decomposed by a single NMF decomposition, and new NMF decompositions were performed in which the previously identified particles were masked out (this also involved finding new suitable values of n). This process was repeated until all phases were identified. This iterative NMF approach allows for NMF to first identify the phases with the highest scattering intensity and subsequently identifying more weakly scattering phases. Results from SVD and the iterative NMF are shown in Section S3 in the supplementary material. Lastly, the binary maps were combined using the same prioritisation scheme used in the ground truth phase map creation to produce the final phase map. The workflow used for NMF-based phase mapping is shown in Fig. 3.

3.5. Vector matching

The implementation used for vector matching was written specifically for this work and is based on existing code in *pyxem* and *diffsims*. A relatively simple vector matching approach was suitable in this study since the dataset only contains six unique zone-axis patterns, as explained in Section 2.1. For the five unique precipitate patterns,

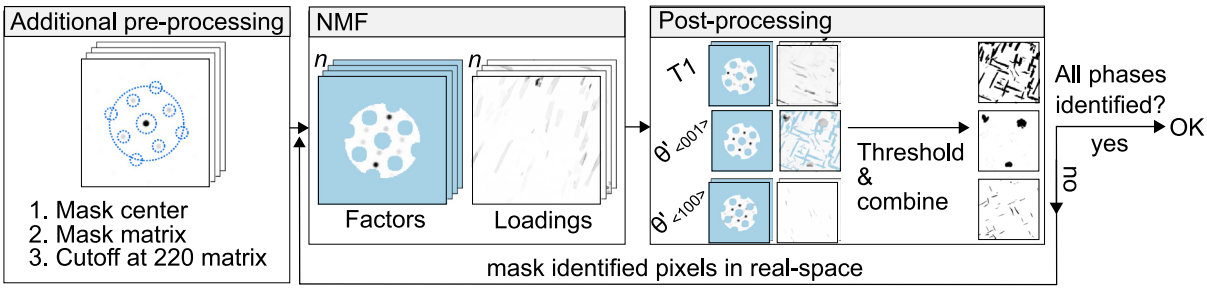

Fig. 3. Schematic illustration of the NMF phase mapping workflow. Al reflections and the direct beam are masked out to enhance the algorithms sensitivity to precipitate reflections and a $\{220\}_{Al}$ cutoff is applied to enhance the importance of low scattering angles. NMF is then performed and resulting components are classified. Loading maps identified as given phases are thresholded and combined into phase maps. These phase maps are used as masks in subsequent NMF decompositions to detect additional phases not detected in the previous decompositions.

reference vectors (k_x, k_y) were calculated for their Bragg spots. For this, the reciprocal lattice of each phase was calculated and rotated to zone axis as explained in Section 3.3. The lattices were rotated in-plane according to the average in-plane rotation of the Al matrix in the pre-processed dataset. Reciprocal lattice points lying within a thin slab centred on the plane $z = 0$ were then taken as the reference vectors. The slab thicknesses, $\triangle z$, were set to 0.030 $Å^{-1}$ and 0.300 $Å^{-1}$ for T_1 and θ', respectively.

Laplacian of Gaussian blob finding was used to detect the Bragg peaks in the pre-processed dataset. The peak positions, given as vectors (k_x, k_y), were subsequently refined using a COM approach. One pattern was selected that only contained Bragg spots from Al, and that was used as reference Al vectors. All vectors located close to the reference Al vectors were removed from each pattern, so that only precipitate Bragg spots not overlapping with Al remained. Patterns with less than two vectors were categorised as Al. For all other patterns, phase identification was performed by comparing the experimental vectors to the precipitate reference vectors. Since many of the precipitates were thin and showed as few as two Bragg spots, it was important to avoid penalising patterns with a low number of vectors. Therefore, a reference vector subset was explicitly made for each experimental pattern. This was done by iterating through the experimental vectors and adding to the subset only the reference vector that it was located closest to.

Subsequently, a comparison was done between each experimental vector set and its corresponding reference vector subset, by calculating a matching score given by: $\Sigma_i(|\vec{u}_i - \vec{v}_i|)/N_v$, where the sum runs over the i vectors. $|\vec{u}_i - \vec{v}_i|$ is the distance between the experimental vector $\vec{u}_i$ and its corresponding reference vector $\vec{v}_i$, while N_v is the number of unique reference vectors. The number of unique reference vectors was taken into account to penalise cases where more than one experimental vector matched the same reference vector. Overall, the reference subset that best matched the experimental vector set was the one giving the lowest score. For cases where the lowest score was above a threshold value of 0.07, the phase was set to 'not indexed'. Such regions typically contained phases that were overlapping along the viewing direction. Fig. 4 illustrates the vector matching workflow used.

3.6. Template matching

Prior to template matching, the pre-processed dataset was additionally subjected to background subtraction based on the difference of Gaussians method in *pyxem*. A mask was also applied to remove the Al lattice and the direct beam (See Section S4.1 in the supplementary material). Both the experimental and the simulated patterns were then subjected to the logarithmic transform as given in Eq. (3) ($a = 0.001$), before a constant value of 0.05 was subtracted from each pattern. These processing steps are further explained and illustrated in Section S4.1 in the supplementary material.

For template matching, the implementation in *pyxem*, developed by Cautaerts et al. [18], was used. First, a template library was created that contained simulated patterns calculated for θ' and T_1 using *diffsims*, as explained in Section 3.3. The maximum excitation error, $\max\{s\}$, was set to 0.030 $Å^{-1}$, 0.050 $Å^{-1}$ and 0.022 $Å^{-1}$ for $\theta'_{\langle 100\rangle}$, $\theta'_{[001]}$ and T_1, respectively, and the choice of these values is discussed in Section S4.2 in the supplementary material. An initial list of beam directions to simulate patterns for, corresponding to Euler angles $(0, \Phi, \phi_2)$, was made by evenly sampling orientations, (Φ, ϕ_2), across the fundamental zones of the two crystal systems with an angular resolution of 0.5° following the route suggested in Ref. [18]. Then, the list was reduced to only include beam tilts, ϕ_T, within 3° from the expected zone axes. This reduced the number of orientations from around 28,500 to 202.

During template matching, each processed experimental pattern is compared to all the simulated patterns after conversion to polar coordinates, (r, ϕ). The comparison is done via the normalised cross-correlation, given by [18,59]:

$$Q(i,\phi) = \frac{\sum_i \sum_j P(x_i, y_j) T(x_i, y_j, \phi)}{\sqrt{\sum_i \sum_j P(x_i, y_j)^2 \sum_i \sum_j T(x_i, y_j, \phi)^2}}, \tag{4}$$

where the sums go over every peak in the simulated patterns. $P(x_i, y_j)$ is the intensity of pixel (i, j) in the experimental pattern, and $T(x_i, y_j, \phi)$ is the intensity of pixel (i, j) in the template rotated to an in-plane angle of $\phi \in (1°, 360°)$. The correlation score, Q, was calculated between each template and each experimental pattern with respect to the azimuth, ϕ, by sliding the template across the experimental pattern. The maximum Q defined the final in-plane angle, ϕ_1, of the template. The ϕ step size, i.e. resolution, was set to 1°. This procedure was repeated for every template, and the template that best matched the experimental pattern, i.e. that with highest Q, determined the phase and orientation assigned to the experimental pattern. Since the Al Bragg spots were masked out in the experimental patterns and the template bank did not include simulations of Al, the Al regions in the initial phase map were assigned to precipitates with low correlation scores. A final phase map that included Al was made by superimposing a mask onto the initial phase map corresponding to the Al region, which was made by thresholding the correlation score map.

The template matching processing workflow is schematically depicted in Fig. 5.

3.7. Artificial neural network

3.7.1. Simulating training data for artificial neural networks

For the ANN approach, 10.000 simulated patterns were created per phase. The simulation parameters were varied randomly following a uniform distribution between min/max to ensure sufficient variation in the data. Both the azimuth angle ϕ_A and the tilt angle ϕ_T, defined as the rotation away from zone axis, were varied along with the maximum excitation error $\max\{s_g\}$. To account for strain, the lattice parameter of Al was chosen randomly from a normal distribution according to:

$$f(x) = \frac{1}{\sigma\sqrt{2\pi}} e^{-\frac{1}{2}\left(\frac{x-\mu}{\sigma}\right)^2}, \tag{5}$$

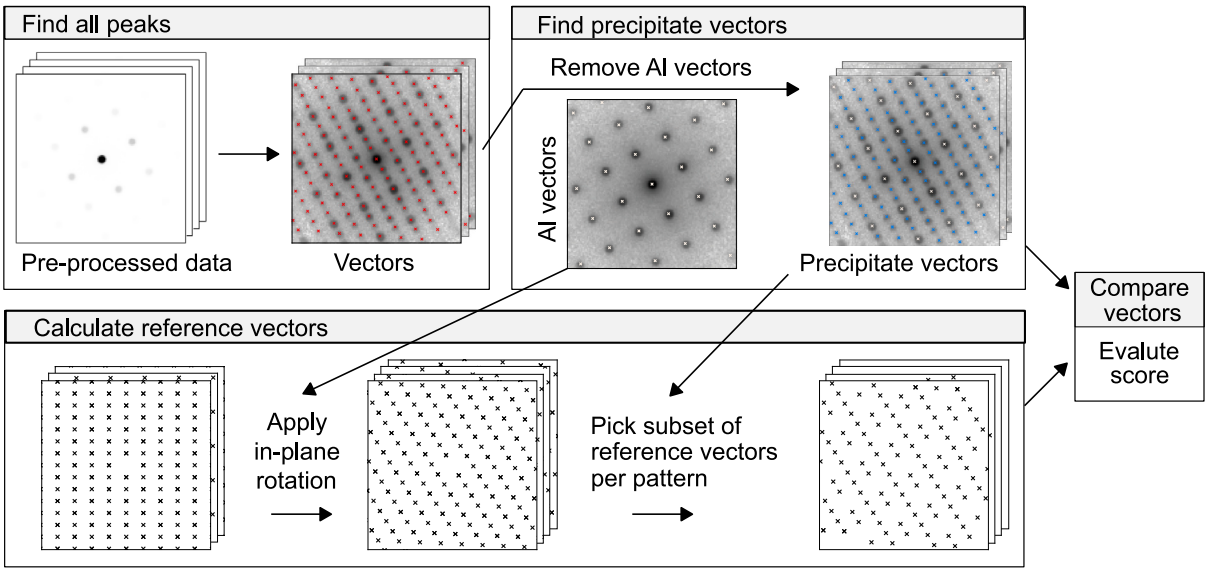

Fig. 4. Illustration of the vector matching workflow. Peak finding is applied to the pre-processed data to find all Bragg peaks, i.e. vectors. The Al vectors are removed from the set of experimental vectors to give only the precipitate vectors. Reference vectors are calculated for the precipitates, and the in-plane rotation found from Al vectors is applied to these reference vectors. Subsets of reference vectors are created for each pattern based on its corresponding experimental vectors before the reference subsets are compared to the experimental precipitate vectors.

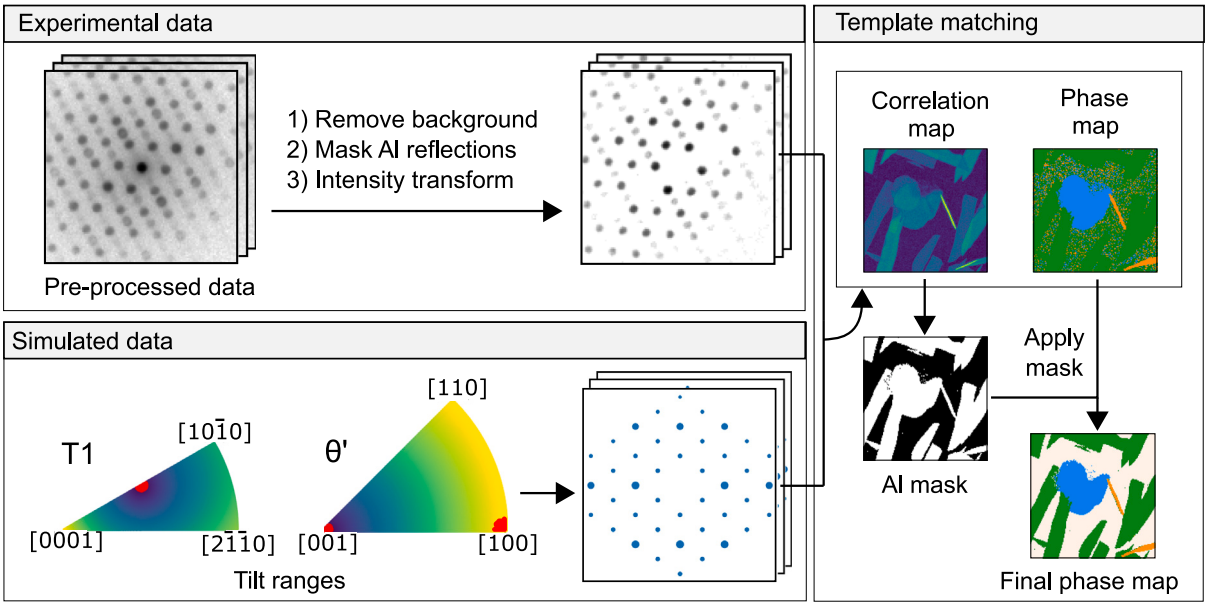

Fig. 5. Schematic workflow for template matching. A Difference of Gaussians background subtraction was performed, before Al reflections were masked and a logarithmic transform (Eq. (3)) was applied. Next, simulations of diffraction patterns were made for each precipitate phase within a beam tilt range of 3°. The red dots in the inverse pole figures indicate the orientations of the precipitates. The simulations were compared to the experimental data via the normalised cross-correlation to find the best matches and get the initial phase map. An Al mask was made from the correlation score map and applied to the template matching results to get the final phase map.

where $\mu = 4.040$ Å is the expectation value and $\sigma = 0.007$ Å is the standard deviation.

The diffraction patterns from Al and the precipitate phases were simulated independently with the same ϕ_A and ϕ_T. All of the precipitates were embedded in Al, hence all diffraction patterns stemming from precipitate regions also include the Al reflections in addition to the unique precipitate reflections. To account for this, the Al and precipitate pattern were added together with a weighting parameter, w, according to: $(\mathrm{DP}_{\mathrm{Al}} + w \cdot \mathrm{DP}_{\mathrm{precipitate}})$, where $\mathrm{DP}_{\mathrm{Al}}$ and $\mathrm{DP}_{\mathrm{precipitate}}$ are the Al and the precipitate diffraction pattern, respectively. To provide variation in the diffracted intensities, various data augmentation techniques were applied to the simulated diffraction patterns. The data augmentation is summarised as follows in chronological order:

1. **Size of the reflections**: Each Bragg spot was represented by a Gaussian with varying standard deviation.
2. **Weighting between Al- and precipitate diffracted intensities** were varied to mimic the effect of varying precipitate sizes.
3. **Poisson noise**: To mimic detector shot noise, Poisson noise was added to the patterns.
4. **Gaussian noise**: To mimic inelastic and diffuse scattering and detector noise, Gaussian noise was added.
5. **Radial gradient**: To mimic inelastic and diffuse scattering around the central beam, a radially decaying background was added to the patterns. Both the maximum intensity and spread of the radial gradient were varied.

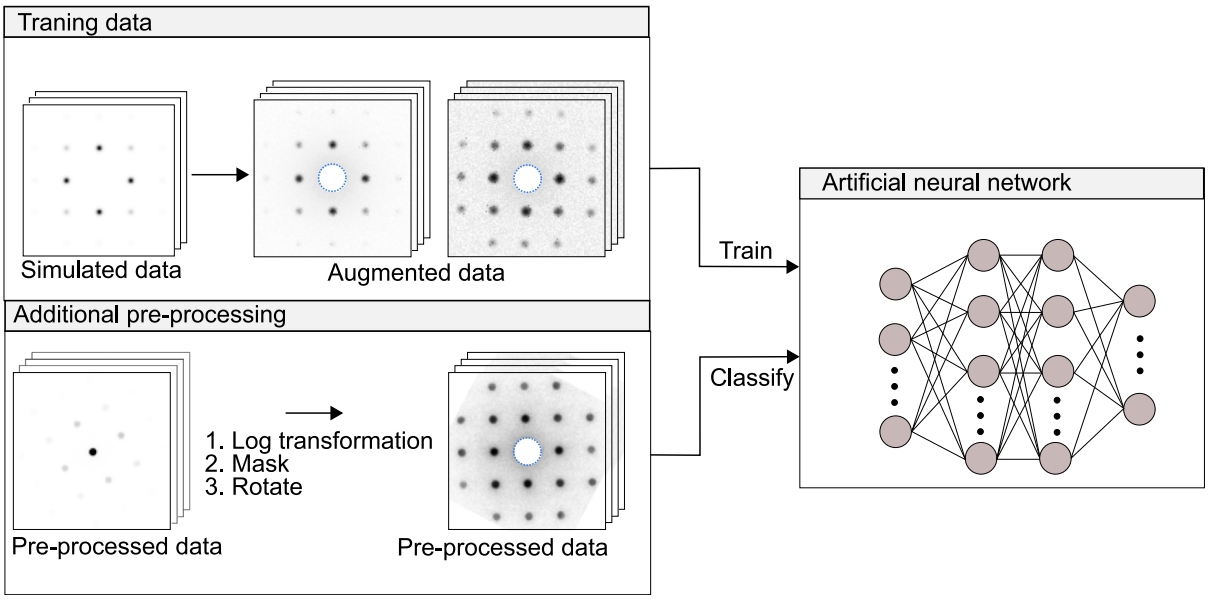

Fig. 6. Workflow for the ANN approach. Training data is created by simulating diffraction patterns and augmenting the simulations. The experimental data was subjected to a log transform, the direct beam was masked out, and the data stack was rotated to $\phi_A \approx 0$.

6. **Log transform**: To vary the intensities in the simulated diffraction patterns, a log transform was executed according to Eq. (3) with a varying randomly.

Prior to training, each simulated pattern was normalised so that all pixel intensities lay between 0 and 1, and the simulated database was split into training-, validation and test datasets [60]. 80% of the data was reserved for the training set, while the last 20% was equally shared between the validation and test sets.

3.7.2. Training the artificial neural network

The ANN was implemented using the python library *TensorFlow* [61] and consisted of three layers: input layer, hidden layer and output layer. The 128x128 pixels simulated diffraction patterns were passed to the input layer. The output layer predicts the crystal phase for each input image. The learning curve obtained from the ANN is shown in Fig. S14 in the supplementary material.

In addition to the pre-processing steps presented in Section 3.1, the experimental data underwent the log transform in Eq. (3) with $a = 0.024$. The central beam was masked out both in the training data and in the experimental data. The experimental data stack was rotated so that the azimuth angle ϕ_A was approximately zero by rotating $\phi_A = -29.65°$ counter clock-wise, as obtained from the vector matching. This was done to avoid rotating the simulated patterns to increase the generality of the trained ANN. The workflow is schematically shown in Fig. 6.

4. Results

4.1. Overview of dataset A

An overview of Dataset A is shown in Fig. 7. The BF image in (a) shows the presence of precipitates with different morphologies. In (b), a VDF image from the same region as in Fig. 7(a) is shown. The placement of the virtual aperture is indicated by the red circle in (d). The yellow circle in the VDF indicates a region where two precipitates overlap. The ground truth phase map is shown in (c). The coloured rectangles in (b) indicate pixels where the diffraction patterns in Fig. 7(d)–(g) originate from. The PED patterns in Fig. 7(d)–(g) correspond to Al, $\theta'_{\langle 100\rangle}$, $\theta'_{[001]}$ and T_1, respectively and are taken from regions indicated by the beige, orange, blue and green rectangle in Fig. 7(b). Another orientation (not shown) exists for T_1 and $\theta'_{\langle 100\rangle}$ which can be obtained by rotating the precipitate reflections 90°. Simulated diffraction patterns corresponding to the experimental patterns in Fig. 7(c)–(f) are shown in Figure S15 in the supplementary material. A similar overview of Dataset B is given in Section S1 in the supplementary material.

It is evident from the VDF image (Fig. 7(b)) that the different precipitate categories can be separated based on the combination of their morphology and orientation within the Al matrix. Both T_1 and θ' are plate-like, but their projected width along $\langle 001\rangle_{Al}$ and orientation differ, making it trivial to separate them in this projection. T_1 has the projected major axis along $[110]_{Al}$ and $[1\bar{1}0]_{Al}$, while the projected major axis of $\theta'_{\langle 100\rangle}$ is along $[100]_{Al}$ and $[010]_{Al}$. The projected width of T_1 is also larger than that of $\theta'_{\langle 100\rangle}$. $\theta'_{[001]}$ grows along the beam direction $[001]_{Al}$ and is roughly circular in shape.

4.2. Phase mapping

Phase maps and difference maps for all the four approaches are shown in Fig. 8. The difference maps were created by taking the difference between the ground truth in Fig. 7(c) and the constructed phase map obtained from each approach. The phase maps for NMF, vector matching, template matching and ANN are shown in Fig. 8(a)–(d), while the difference maps are shown in Fig. 8(e)–(h), respectively. The white pixels in the difference maps indicate mislabelled pixels. Enlarged regions of each phase maps are shown in Fig. 8(i)–(l) corresponding to the region marked by the rectangle in Fig. 8(a).

5. Discussion

A large number of decisions go into producing a phase map, specific for each approach. To aid clarity of the present work, the discussion is split into two sections. In Section 5.1, the phase mapping approaches are discussed in terms of their ease of use and general performance. In Section 5.2, the variations between the approaches will be discussed in terms of the case study done in this work.

All four approaches considered in this manuscript yielded satisfactory accuracies (i.e. > 98%) for Dataset A. It should be noted that in the current work, precession was applied. Experiments conducted without precession may see different trends between the methods.

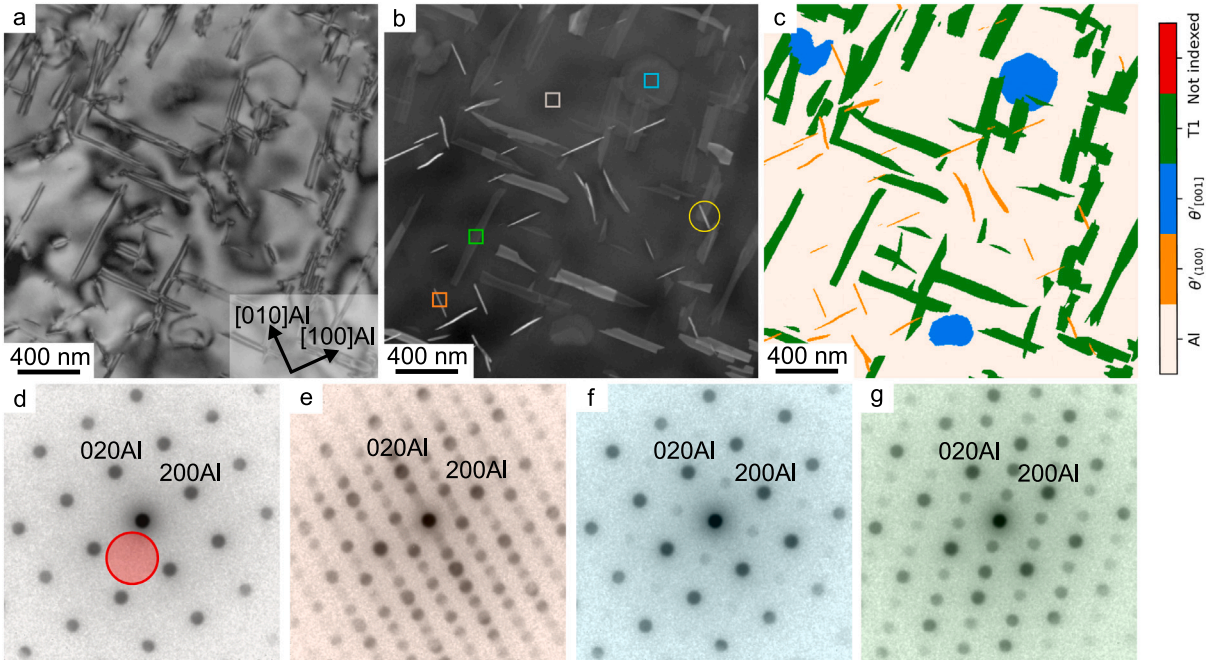

Fig. 7. Overview of Dataset A. **(a)**: BF image of the scanned region. **(b)**: VDF image of the dataset. The placement of the virtual aperture is indicated by the red circle in **(d)**. The yellow circle indicates a region with overlap between two different phases as discussed in the main text. **(c)**: The ground truth phase map. The coloured rectangles in **(b)** indicate regions where the experimental patterns in **(d)-(g)** were collected from, and correspond to Al, $\theta'_{\langle 100\rangle}$, $\theta'_{[001]}$ and T_1, respectively. Diffraction patterns are presented on a log scale for visual clarity.

Precession has previously been found to be advantageous for lowering the number of components needed for NMF [32]. It also provides better peak finding due to improved uniformity of the disk intensities. Similarly, the template matching and ANN approaches relied on kinematical diffraction simulations benefit from precession [9]. Despite this consideration, it is reasonable to assume that the conclusions are still broadly applicable to 4D-STEM experiments without precession.

5.1. Strengths and weaknesses of the four approaches

5.1.1. Non-negative matrix factorisation

In line with previous studies [32,37,38,40,41,62], the NMF based approach provided a solid route to construct phase maps for cases with a small number of distinct phase patterns. In this work results from a sequential approach for using NMF that relied on iteratively excluding probe positions that had been accurately decomposed in the previous step was introduced. This allowed patterns with weak reflections to be better represented in the resulting phase maps. Without iteratively excluding the probe positions labelled in the previous step, a high number (> 20 in the present case) of components are typically required to successfully decompose the weaker signals.

The sensitivity of NMF to weak reflections depends on the occurrence of similar patterns through the dataset. A weak scattering signal, such as the one for $\theta'_{[001]}$ precipitates, can be balanced by a high number of datapoints exhibiting the same weak signal. This is one of the advantages of NMF, by combining information from several scan positions, the resulting NMF components typically exhibit a higher signal-to-noise ratio when compared to the raw data. This is in contrast to the other approaches used in this study that analyse the diffraction patterns one-by-one without taking advantage of the fact that there are only a few unique patterns in the data. If however there are large variations in the diffracted intensities within one group - e.g. due to strain or multiple grains - NMF will require a large number of components to decompose the data and the post-processing will become complicated. In the present case, this is seen as mislabelling some $\theta'_{\langle 100\rangle}$ precipitates as $\theta'_{[001]}$ along their edges. While some of this mislabelling can be accounted for by optimising and applying more advanced thresholding and segmentation algorithms when creating phase maps from the loading maps, it remains a source of error and uncertainty in the method. The main drawback of the NMF based approach is therefore the complexity arising from the combination of the black-box nature of NMF with the large number of manual, user-dependent steps (pre-processing steps involving masking, determining n, initialisation, labelling of components and thresholding).

It is worth noting that in the current implementations, NMF is the only one proven to handle overlapping phases along the viewing direction [33,36], making it favourable when overlap is a major concern. In addition, being an unsupervised learning method, it is the only method that can handle phase mapping tasks with limited prior knowledge of candidate phases/orientations, since the other approaches rely on diffraction simulations.

5.1.2. Vector matching

Variations on vector matching approaches have been published a number of times [19–22]. In this work, the vector matching was implemented from scratch, taking advantage of the well-defined orientation relationships between the Al host lattice and the precipitates. Vector based approaches require accurate pattern calibration and centring of the direct beam. Perhaps most challenging, decent results rely on an accurate peak-finding method is implemented, ideally one that can detect weak Bragg peaks while simultaneously avoiding mislabelling background noise. The peak finding step is also the most computationally intensive step of the vector matching process. The algorithm was sensitive enough to find weak diffracted intensities, and the vector matching also works well when only as few as two diffracted reflections stemmed from precipitates.

The current implementation of the vector matching approach lacks the complexity to handle overlapping phases, and did not use the phase prioritisation scheme explained in Section 3.2. Because of this, the approach struggled with patterns from overlap and interface areas, as can be seen in Fig. 8(b) and (f). This was especially prominent for the interfaces of $\theta'_{\langle 100\rangle}$ precipitates, where mislabelling happened despite the method successfully labelling patterns with as few as two T_1 precipitate vectors. Hence, the main challenge was not the low number

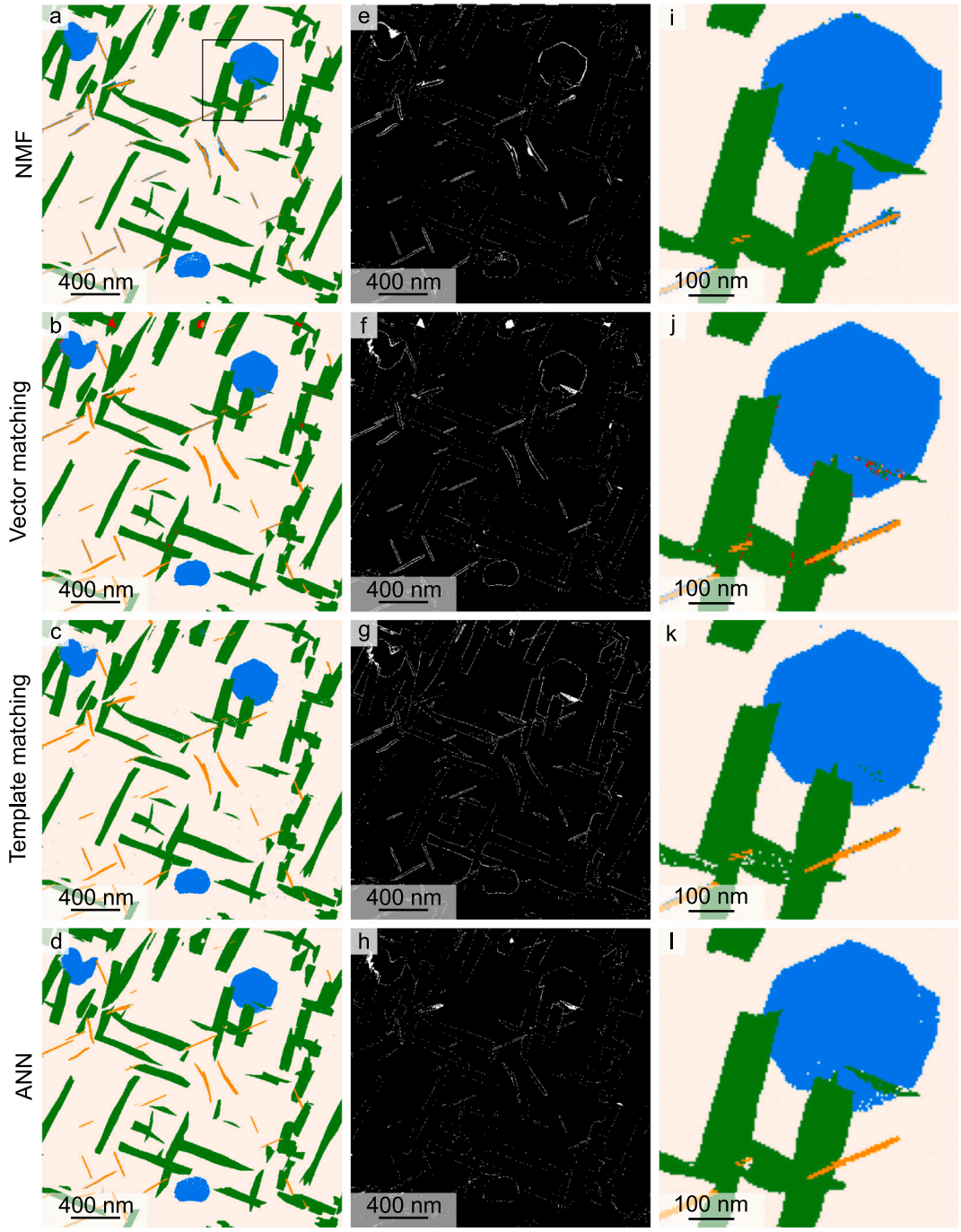

Fig. 8. Phase maps and difference maps from the four phase mapping approaches. **(a)–(d)**: Phase maps for NMF, vector matching, template matching and ANN, respectively. **(e)–(h)**: Difference maps for NMF, vector matching, template matching and ANN, respectively. White pixels indicate mislabelled pixels. **(i)–(l)**: Enlarged regions corresponding to the rectangle in **(a)** of the phase maps in **(a)–(d)**.

of detected vectors in interface patterns, but rather shifts in the Bragg peak positions due to strain. Such features are difficult to treat in this approach due to the scoring strategy. The overlapping patterns could in principle be taken into account by keeping track of the different phases exhibiting a score below a certain threshold, but this was beyond the scope in the current work. Figure S13 of the supplementary material shows a score map, highlighting regions where the method rendered a low score, and it also shows and discusses example patterns from overlap and interface areas.

5.1.3. Template matching

Template matching is routinely used for orientation mapping based on 4D-STEM data [12,13,18]. In this work, prior knowledge was made us of, such as orientation relationships between host lattice and precipitates. These strongly limits the number of entries in the simulation libraries.

In the current work, performing basic pre-processing including centring of the central beam, logarithmic intensity transformation and normalisation of the intensities, culminated in an accuracy of 86.24%. By including background subtraction, the accuracy was significantly

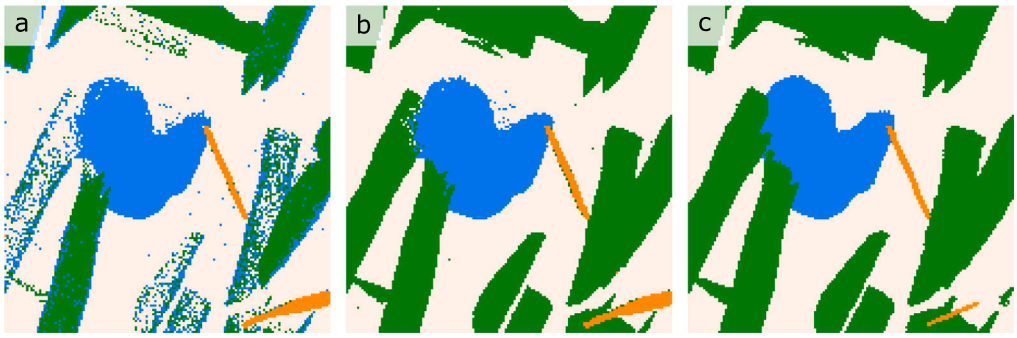

Fig. 9. Phase map from a cropped out region of the full dataset, obtained after using various $\max\{s\}$ values in the simulations. (a) Phase map with $\max\{s\} = 0.01$ Å^{-1} for all phases. (b) Phase map with $\max\{s\}$ values optimised on a phase-by-phase case: 0.03 Å^{-1}, 0.05 Å^{-1} and 0.022 Å^{-1} for respectively $\theta'_{\langle 100\rangle}$, $\theta'_{[001]}$ and T_1. (c) Ground truth map of the same area.

improved to 98.24%. A comparison between the results obtained with basic pre-processing and more complex pre-processing is shown in Section S4 in the supplementary material. This user involvement reduces the ease of use of working with template matching and also the objectiveness.

A challenge when doing phase mapping of embedded phases is that the reflections of the embedded phases might be weak compared to the reflections from the host material. As seen in this work, template matching struggled with patterns exhibiting such characteristics. Differentiating between T_1 and Al regions with low correlation scores, was challenging. This was overcome by optimising the $\max\{s\}$ parameter for each phase individually, as illustrated in Fig. 9. This enabled the generation of a phase map that matches the ground truth phase map in Fig. 9c. Background subtraction and the optimisation of the $\max\{s\}$ parameter are often performed iteratively, by comparing the produced phase map with the VDF image, or if applicable, a ground truth phase map. A more detailed description of the selection of $\max\{s\}$ values is presented in Section S4.2 in the supplementary material.

5.1.4. Artificial neural networks

Neural networks has gained enormous momentum in analysing TEM experiments in recent years [4,26,27,42] due to the increase in data sizes and also an increased availability of computing resources. An important consideration when implementing an ANN is the design of the training set [63]. Great care must be taken during the creation of simulated training data. In this study, variable simulation parameters were used to create suitable training data.

In addition to varying the simulation parameters, the resulting simulated diffraction patterns underwent several image transformations to augment the data. Adding noise is considered to be the most critical data augmentation step. If noise is not added, the ANN labelled almost all the PED patterns as T_1, since the T_1 training data had the lowest minimum weighting parameter. This is expected, since the ANN in this scenario learns that only precipitates have intensity between the Bragg spots stemming from Al.

A major advantage of using ANN is that once the network is trained, the classification is fast and accurate. It also performs well on weak diffracted intensities, which can be taken into account by adjusting the weighting between the Al reflections and the precipitate reflections. When properly trained, the same ANN can be applied on datasets from the same material system acquired at different TEM sessions as well, as discussed in Section 5.1.5.

In this work, simulated patterns were used as training data. Labelled experimental patterns could in principle be used as input for the training instead of simulated patterns. For some samples, this could be performed following the same approach as used in the current work for the creation of the ground truth image. In general however, this is not always possible with satisfactory accuracy and one would have to rely on other approaches to label the experimental data, e.g. NMF, vector matching or template matching. One would also have to obtain data from several regions of the sample or even obtain data from several samples to account for e.g. sample tilt, different thicknesses, alignment of the microscope and so on.

5.1.5. Applicability of the approaches on similar datasets

Dataset B, presented in Section S1 in the supplementary material, was collected to investigate the applicability of the approaches on other datasets from the same sample. When it comes to the NMF approach, the same number of iterations was required as for Dataset A, to successfully separate the signals from the different precipitates. Moreover, the thresholding of the components was modified. Hence, the parameters of the NMF based approach needed to be tailored to fit with the new experimental conditions. Once the parameters were determined, the resulting phase map was the most convincing one when qualitatively comparing it to the VDF image. The vector matching and ANN approaches also perform adequately on Dataset B and are good approaches to choose if the phase mapping is done routinely. In that regard, the ANN is the fastest, since for vector matching one would need to perform peak finding. For the template matching however, the phase map exhibits speckled noise in the Al matrix to a more severe extent than in the phase map of Dataset A. To increase the quality of the phase map from Dataset B, it is assumed that optimising the $\max\{s\}$ would be advantageous, showcasing that using the same template library on two different datasets might not always be optimal.

In the current use case, only six unique diffraction patterns were present in the data. Few unique patterns are often expected in materials where semi-coherent secondary phases are embedded in a host material, since such phases often exhibit a fixed orientation relationship with the matrix. However, for polycrystalline materials a higher number of unique patterns must be considered. Both NMF, template matching and ANNs have demonstrated robustness, even in more complex applications, as exemplified in Refs. [34,36] for grain mapping using NMF, Refs. [12,13,18] for template matching based orientation mapping and [42] for orientation mapping using ANN. It is important to note that the vector matching algorithm discussed in the current work was designed to handle zone-axis patterns.

5.2. Trends appearing in the case study

All four approaches detailed in this work yielded accuracies of 98.5% ± 0.5% (see Table 3) when compared against the ground truth phase map. It is noted that the ground truth phase map was created manually, so that the small differences in accuracies are not significant. While some decisions made during this study (e.g. distortion corrections were not applied) will have variable effects dependent on the chosen method, it has been demonstrated that all four methods can produce highly accurate phase maps. In this section, the risk of failure for each of the approaches will be elucidated.

Table 3
Comparison of the four phase mapping approaches employed in this work in terms of accuracy, defined as the deviation from the ground truth phase map.

	NMF	Vector matching	Template matching	ANN
Accuracy (%)	98.50	98.46	98.25	99.04

The majority of mislabelled pixels for all methods occurred at the edges of precipitates. This can be seen visually by inspecting the middle column of Fig. 8. Such errors are relatively harmless when evaluating phase maps, but is more severe if particle sizing or volume fractions are sought. However, given the overlapping nature of the patterns, correctly discerning an edge (either automatically or manually) is always likely to be contentious. It should also be noted that the ground truth phase map is also created manually and there is no guarantee that this phase map more accurately captures the precipitate interfaces as compared to the phase maps from the other methods.

More interesting are the subtle differences in errors the routines make. The template matching routine, for example, exhibits speckle noise (i.e. single mislabelled pixels within the matrix) not seen in the other approaches. Like the errors at the interfaces, this is harmless when inspecting the phase maps, since a sensible user will understand that it is an error and not a finely distributed arrays of nanometer sized precipitates. For phase fractionation however, this is more severe. Because such mislabelling is unlikely to be random, it may form clusters in other representations (eg. orientation maps such as those in Ref. [64]) which will be misleading. The speckle noise can in principle be removed by post processing by e.g. removing all single pixels or kernel smoothing.

Both rule-based approaches (template matching and vector matching), and to some extent ANN struggle in the region with overlapping $\theta'_{[001]}$ and T_1 highlighted by the right most column of Fig. 8. This problem can also be seen at the boundaries of the $\theta'_{[001]}$ (blue in images) precipitate in the upper left hand corner. One possible explanation for this is that the prioritisation scheme was easily applied in the NMF based approach, which is the approach that tackles these overlap regions best. The rule-based approaches on the other hand are deterministic, since these approaches were not implemented to tackle overlap.

Although these difference are interesting, and may be a reasonable motivation for selecting one method over another, in general others would be better served by selecting an approached based on the comments in Section 5.1.

6. Conclusion

In this work four data analysis approaches for phase mapping of precipitates with fixed orientation relationships in Al alloys were employed and compared using a dataset acquired from an Al-Cu-Li alloy containing two different precipitate phases embedded in Al. Diffraction patterns from probe positions containing precipitates show strong reflections from the matrix which creates an added challenge to the phase identification regimes. In this case, the precipitates have different morphologies making them separable in virtual images. This allowed for the creation of a ground truth phase map which was used to estimate the accuracy of the automated phase mapping results. The approaches evaluated were NMF, vector matching, template matching and ANN. All four approaches performed well on both weak and strong diffracted intensities and achieved satisfactory accuracy with less than 2% of the pixels mislabelled. Most mislabelled pixels stem from regions at the interface between precipitate and Al.

The main results are summarised as follows:

- NMF is the easiest method to get started with, and the component maps produced can aid in initial investigations of a dataset. However, the post-processing required to produce phase maps can be highly involved and user dependent. Alongside this, the method offers some parameters that can easily be erroneously passed to the algorithm, e.g. choosing an incorrect number of components. Such errors can propagate to produce phase maps that might look visually correct, but are physically wrong.
- Once the ANN is trained, the approach is fast, accurate and has a high throughput. Using an ANN has a large set up cost as careful consideration needs to be given to the training dataset.
- The main advantage of vector matching is that it requires little pre- and post-processing of the experimental data. It does however depend on a precise determination of the position of the Bragg spots. The method is relatively new and thus does not have much supporting implementation or literature.
- Template matching requires more upfront pre-processing as compared to vector matching that can have significant effects on the final results. It also had some concerning 'speckle noise' in the study, which may or may not be important to users. These risks may be offset for many less technically inclined users by the well developed ecosystem of support the method has.

CRediT authorship contribution statement

E. Thronsen: Initiated the study, Developed the neural network approach, Drafted the initial manuscript, Commented on the final manuscript. **T. Bergh:** Initiated the study, Implemented the vector-based approach, Significantly contributed to writing, Commented on the final manuscript. **T.I. Thorsen:** Did the template matching, Significantly contributed to writing, Commented on the final manuscript. **E.F. Christiansen:** Initiated the study, Acquired the TEM- and SPED data, Did the NMF decomposition and analysed the decomposed dataset, Significantly contributed to writing, Commented on the final manuscript. **J. Frafjord:** Implemented the vector-based approach, Commented on the final manuscript. **P. Crout:** Assisted in the development of the neural network approach, Commented on the final manuscript. **A.T.J. van Helvoort:** Supervised the research, Commented on the final manuscript. **P.A. Midgley:** Supervised the research, Commented on the final manuscript. **R. Holmestad:** Initiated the study, Supervised the research, Commented on the final manuscript.

Declaration of competing interest

The authors declare the following financial interests/personal relationships which may be considered as potential competing interests: Randi Holmestad reports financial support was provided by Research Council of Norway. Randi Holmestad reports financial support was provided by Horizon Europe.

Data availability

The raw data and models used to reproduce the presented results are available in the Zenodo repository https://doi.org/10.5281/zenodo.6645396 [65]. The implemented codes are openly available at https://github.com/elisathr/SPED-phase-mapping/tree/main [66].

Acknowledgements

This work was supported by the NTNU Digital Transformation initiative 'Alldesign' (E.T. and R.H.). Research Council of Norway (RCN) has supported this work through several projects and centres: InSane (IN-situ Studies of highly conductive bonded interfaces between Aluminium and copper at the Nano-scalE) under contract no. 301176, the iCSI (industrial Catalysis Science and Innovation) centre under contract

no. 237922, AluBridge (Towards robust design and efficient production of durable and sustainable aluminium bridges) under contract no. 314063, SumAl (Solute cluster manipulation for optimised properties in Al-Mg-Si based Al alloys) under contract no. 294933, SFI PhysMet (centre for Research-based Innovation) under contract no. 309584. P.C. acknowledges the support of his studentship from the EPSRC. The TEM experiments were done at the Norwegian centre for transmission electron microscopy (NORTEM) funded by RCN contract no. 197405. The IDUN cluster at the high performance computing group at NTNU is acknowledged for the use of their computing resources in this work [67]. This project has received funding from EU's Horizon 2020 grant no 823717 (ESTEEM3). Dr. Sigurd Wenner is acknowledged for preparing the TEM specimen.

Appendix A. Supplementary data

Supplementary material related to this article can be found online at https://doi.org/10.1016/j.ultramic.2023.113861.

References

[1] S.J. Andersen, C.D. Marioara, J. Friis, S. Wenner, R. Holmestad, Precipitates in aluminium alloys, Adv. Phys.: X 3 (1) (2018) 1479984, http://dx.doi.org/10.1080/23746149.2018.1479984, URL: https://www.tandfonline.com/doi/full/10.1080/23746149.2018.1479984.

[2] T. Bergh, L. Sandnes, D.N. Johnstone, Ø. Grong, F. Berto, R. Holmestad, P.A. Midgley, P.E. Vullum, Microstructural and mechanical characterisation of a second generation hybrid metal extrusion & bonding aluminium-steel butt joint, Mater. Charact. 173 (2021) 110761, http://dx.doi.org/10.1016/J.MATCHAR.2020.110761.

[3] T.D. Ngo, A. Kashani, G. Imbalzano, K.T. Nguyen, D. Hui, Additive manufacturing (3D printing): A review of materials, methods, applications and challenges, Composites B 143 (2018) 172–196, http://dx.doi.org/10.1016/J.COMPOSITESB.2018.02.012.

[4] C. Ophus, Four-dimensional scanning transmission electron microscopy (4D-STEM): From scanning nanodiffraction to ptychography and beyond, in: Microscopy and Microanalysis, Vol. 25, No. 3, Cambridge University Press, 2019, pp. 563–582, http://dx.doi.org/10.1017/S1431927619000497.

[5] J.M. Zuo, R. Yuan, Y.T. Shao, H.W. Hsiao, S. Pidaparthy, Y. Hu, Q. Yang, J. Zhang, Data-driven electron microscopy: electron diffraction imaging of materials structural properties, Microscopy 71 (2022) i116–i131, http://dx.doi.org/10.1093/JMICRO/DFAB032, URL: https://academic.oup.com/jmicro/article/71/Supplement_1/i116/6530493.

[6] J.M. Zuo, J.C. Spence, Advanced Transmission Electron Microscopy: Imaging and Diffraction in Nanoscience, first ed., Springer, 2017, http://dx.doi.org/10.1007/978-1-4939-6607-3.

[7] P.A. Midgley, A.S. Eggeman, Precession electron diffraction – a topical review, IUCrJ 2 (1) (2015) 126–136, http://dx.doi.org/10.1107/S2052252514022283, URL: https://scripts.iucr.org/cgi-bin/paper?ro5004.

[8] R. Vincent, P.A. Midgley, Double conical beam-rocking system for measurement of integrated electron diffraction intensities, Ultramicroscopy 53 (3) (1994) 271–282, http://dx.doi.org/10.1016/0304-3991(94)90039-6.

[9] A.S. Eggeman, R. Krakow, P.A. Midgley, Scanning precession electron tomography for three-dimensional nanoscale orientation imaging and crystallographic analysis, Nature Commun. 6 (1) (2015) 1–7, http://dx.doi.org/10.1038/ncomms8267, URL: https://www.nature.com/articles/ncomms8267.

[10] E.F. Rauch, J. Portillo, S. Nicolopoulos, D. Bultreys, S. Rouvimov, P. Moeck, Automated nanocrystal orientation and phase mapping in the transmission electron microscope on the basis of precession electron diffraction, Z. Kristallogr. 225 (2–3) (2010) 103–109, http://dx.doi.org/10.1524/ZKRI.2010.1205/MACHINEREADABLECITATION/RIS, URL: https://www.degruyter.com/document/doi/10.1524/zkri.2010.1205/html.

[11] I. MacLaren, E. Frutos-Myro, D. McGrouther, S. McFadzean, J.K. Weiss, D. Cosart, J. Portillo, A. Robins, S. Nicolopoulos, E. Nebot Del Busto, R. Skogeby, A comparison of a direct electron detector and a high-speed video camera for a scanning precession electron diffraction phase and orientation mapping, Microsc. Microanal. 26 (6) (2020) 1110–1116, http://dx.doi.org/10.1017/S1431927620024411, URL: https://www.cambridge.org/core/journals/microscopy-and-microanalysis/article/comparison-of-a-direct-electron-detector-and-a-highspeed-video-camera-for-a-scanning-precession-electron-diffraction-phase-and-orientation-mapping/550A9063C10815FE06CB3442F0E5A63.

[12] J. Jeong, N. Cautaerts, G. Dehm, C.H. Liebscher, Automated crystal orientation mapping by precession electron diffraction-assisted four-dimensional scanning transmission electron microscopy using a scintillator-based CMOS detector, Microsc. Microanal. 27 (5) (2021) 1102–1112, http://dx.doi.org/10.1017/S1431927621012538, URL: https://www.cambridge.org/core/journals/microscopy-and-microanalysis/article/automated-crystal-orientation-mapping-by-precession-electron-diffractionassisted-fourdimensional-scanning-transmission-electron-microscopy-using-a-scintillatorbased-cmos-detector.

[13] E.F. Rauch, M. Véron, Automated crystal orientation and phase mapping in TEM, Mater. Charact. 98 (2014) 1–9, http://dx.doi.org/10.1016/J.MATCHAR.2014.08.010.

[14] P. Moeck, S. Rouvimov, E.F. Rauch, M. Véron, H. Kirmse, I. Häusler, W. Neumann, D. Bultreys, Y. Maniette, S. Nicolopoulos, High spatial resolution semi-automatic crystallite orientation and phase mapping of nanocrystals in transmission electron microscopes, Cryst. Res. Technol. 46 (6) (2011) 589–606, http://dx.doi.org/10.1002/CRAT.201000676, https://onlinelibrary.wiley.com/doi/full/10.1002/crat.201000676 https://onlinelibrary.wiley.com/doi/abs/10.1002/crat.201000676 https://onlinelibrary.wiley.com/doi/10.1002/crat.201000676.

[15] G. Brunetti, D. Robert, P. Bayle-Guillemaud, J.L. Rouvière, E.F. Rauch, J.F. Martin, J.F. Colin, F. Bertin, C. Cayron, Confirmation of the domino-cascade model by LiFePO4/FePO4 precession electron diffraction, Chem. Mater. 23 (20) (2011) 4515–4524, http://dx.doi.org/10.1021/CM201783Z/ASSET/IMAGES/CM-2011-01783Z_M004.GIF, URL: https://pubs.acs.org/doi/full/10.1021/cm201783z.

[16] E.F. Rauch, M. Véron, Methods for orientation and phase identification of nano-sized embedded secondary phase particles by 4D scanning precession electron diffraction, Acta Crystallogr. Sect. B Struct. Sci. Cryst. Eng. Mater. 75 (4) (2019) 505–511, http://dx.doi.org/10.1107/S2052520619007583, http://scripts.iucr.org/cgi-bin/paper?je5011 https://journals.iucr.org/b/issues/2019/04/00/je5011/.

[17] L.c. Henry, N. Bernier, M. Jacob, G. Navarro, L. Clément, J.L. Rouvière, E. Robin, Studying phase change memory devices by coupling scanning precession electron diffraction and energy dispersive X-ray analysis, Acta Mater. 201 (2020) 72–78, http://dx.doi.org/10.1016/J.ACTAMAT.2020.09.033.

[18] N. Cautaerts, P. Crout, H.W. Ånes, E. Prestat, J. Jeong, G. Dehm, C.H. Liebscher, Free, flexible and fast: Orientation mapping using the multi-core and GPU-accelerated template matching capabilities in the Python-based open source 4D-STEM analysis toolbox Pyxem, Ultramicroscopy 237 (2022) 113517, http://dx.doi.org/10.1016/J.ULTRAMIC.2022.113517.

[19] S. Zaefferer, New developments of computer-aided crystallographic analysis in transmission electron microscopy, J. Appl. Crystallogr. 33 (1) (2000) 10–25, http://dx.doi.org/10.1107/S0021889899010894.

[20] M. Klinger, A. Jäger, Crystallographic tool box (CrysTBox): Automated tools for transmission electron microscopists and crystallographers, J. Appl. Crystallogr. 48 (2015) (2015) 2012–2018, http://dx.doi.org/10.1107/S1600576715017252.

[21] M. Yifei, Z. Jian-min, Improvements in electron diffraction pattern automatic indexing algorithms, in: The 16th European Microscopy Congress, Vol. 10701, EMC 2016, 2017, pp. 1–8, http://dx.doi.org/10.1051/epjap/2017160444.

[22] C. Li, X. Li, R. Kirian, J.C. Spence, H. Liu, N.A. Zatsepin, SPIND: A reference-based auto-indexing algorithm for sparse serial crystallography data, IUCrJ 6 (2019) 72–84, http://dx.doi.org/10.1107/S2052252518014951.

[23] G.W. Paterson, R.W. Webster, A. Ross, K.A. Paton, T.A. MacGregor, D. McGrouther, I. MacLaren, M. Nord, Fast pixelated detectors in scanning transmission electron microscopy. part II: Post-acquisition data processing, visualization, and structural characterization, Microsc. Microanal. Off. J. Microsc. Soc. Am. Microbeam Anal. Soc. Microsc. Soc. Canada 26 (5) (2020) 944–963, http://dx.doi.org/10.1017/S1431927620024307, URL: https://pubmed.ncbi.nlm.nih.gov/32883393/.

[24] C. Wejdemann, H.F. Poulsen, Multigrain indexing of unknown multiphase materials, J. Appl. Crystallogr. 49 (2) (2016) 616–621, http://dx.doi.org/10.1107/s1600576716003691.

[25] A. Morawiec, Indexing of diffraction patterns for determination of crystal orientations, Acta Crystallogr. Sect. A Found. Adv. 76 (6) (2020) 719–734, http://dx.doi.org/10.1107/S2053273320012802/TEXIMAGES/IV5009FI229.GIF, http://scripts.iucr.org/cgi-bin/paper?iv5009 https://journals.iucr.org/a/issues/2020/06/00/iv5009/.

[26] S.V. Kalinin, M. Ziatdinov, S.R. Spurgeon, C. Ophus, E.A. Stach, T. Susi, J. Agar, J. Randall, Deep learning for electron and scanning probe microscopy: From materials design to atomic fabrication, MRS Bull. 47 (9) (2022) 931–939, http://dx.doi.org/10.1557/S43577-022-00413-3/FIGURES/3, URL: https://link.springer.com/article/10.1557/s43577-022-00413-3.

[27] M. Botifoll, I. Pinto-Huguet, J. Arbiol, Machine learning in electron microscopy for advanced nanocharacterization: current developments, available tools and future outlook, Nanoscale Horizons 7 (12) (2022) 1427–1477, http://dx.doi.org/10.1039/D2NH00377E, https://pubs.rsc.org/en/content/articlehtml/2022/nh/d2nh00377e https://pubs.rsc.org/en/content/articlelanding/2022/nh/d2nh00377e.

[28] W. Xu, J.M. LeBeau, A deep convolutional neural network to analyze position averaged convergent beam electron diffraction patterns, Ultramicroscopy 188 (2018) 59–69, http://dx.doi.org/10.1016/J.ULTRAMIC.2018.03.004.

[29] K. Kaufmann, C. Zhu, A.S. Rosengarten, K.S. Vecchio, K.S. Vecchio, Deep neural network enabled space group identification in EBSD, Microsc. Microanal. Off. J. Microsc. Soc. Am. Microbeam Anal. Soc. Microsc. Soc. Canada 26 (3) (2020) 447–457, http://dx.doi.org/10.1017/S1431927620001506, URL: https://pubmed.ncbi.nlm.nih.gov/32406353/.

[30] D. Dhall, R. Kaur, M. Juneja, Machine learning: A review of the algorithms and its applications, in: IRIC 2019, Vol. 597, Springer, 2020, pp. 47–63, http://dx.doi.org/10.1007/978-3-030-29407-6_5/TABLES/2, URL: https://link.springer.com/chapter/10.1007/978-3-030-29407-6_5.

[31] D.D. Lee, H.S. Seung, Learning the parts of objects by non-negative matrix factorization, Nature 401 (6755) (1999) 788–791, http://dx.doi.org/10.1038/44565, URL: www.nature.com.

[32] B.H. Martineau, D.N. Johnstone, A.T. van Helvoort, P.A. Midgley, A.S. Eggeman, Unsupervised machine learning applied to scanning precession electron diffraction data, Adv. Struct. Chem. Imaging 5 (1) (2019) 1–14, http://dx.doi.org/10.1186/s40679-019-0063-3.

[33] T. Bergh, D.N. Johnstone, P. Crout, S. Høgås, P.A. Midgley, R. Holmestad, P.E. Vullum, A.T. Helvoort, Nanocrystal segmentation in scanning precession electron diffraction data, J. Microsc. 279 (3) (2020) 158–167, http://dx.doi.org/10.1111/JMI.12850, https://onlinelibrary.wiley.com/doi/full/10.1111/jmi.12850 https://onlinelibrary.wiley.com/doi/abs/10.1111/jmi.12850 https://onlinelibrary.wiley.com/doi/10.1111/jmi.12850.

[34] F.I. Allen, T.C. Pekin, A. Persaud, S.J. Rozeveld, G.F. Meyers, J. Ciston, C. Ophus, A.M. Minor, Fast grain mapping with sub-nanometer resolution using 4D-STEM with grain classification by principal component analysis and non-negative matrix factorization, Microsc. Microanal. 27 (4) (2021) 794–803, http://dx.doi.org/10.1017/S1431927621011946, URL: https://www.cambridge.org/core/journals/microscopy-and-microanalysis/article/fast-grain-mapping-with-subnanometer-resolution-using-4dstem-with-grain-classification-by-principal-component-analysis-and-nonnegative-matrix-factorization/B4E553B8FA99445B8E8BB74A4956FA14.

[35] F. Uesugi, S. Koshiya, J. Kikkawa, T. Nagai, K. Mitsuishi, K. Kimoto, Non-negative matrix factorization for mining big data obtained using four-dimensional scanning transmission electron microscopy, Ultramicroscopy 221 (2021) 113168, http://dx.doi.org/10.1016/J.ULTRAMIC.2020.113168.

[36] A. Bruefach, C. Ophus, M.C. Scott, Analysis of interpretable data representations for 4D-STEM using unsupervised learning, Microsc. Microanal. 28 (6) (2022) 1998–2008, http://dx.doi.org/10.1017/S1431927622012259, URL: https://www.cambridge.org/core/journals/microscopy-and-microanalysis/article/abs/analysis-of-interpretable-data-representations-for-4dstem-using-unsupervised-learning/F6C3034A343672A4C11C4AEDE6C37B94.

[37] J.K. Sunde, C.D. Marioara, A.T. van Helvoort, R. Holmestad, The evolution of precipitate crystal structures in an Al-Mg-Si(-Cu) alloy studied by a combined HAADF-STEM and SPED approach, Mater. Charact. 142 (2018) 458–469, http://dx.doi.org/10.1016/j.matchar.2018.05.031, http://arxiv.org/abs/1805.11910.

[38] J.K. Sunde, C.D. Marioara, R. Holmestad, The effect of low Cu additions on precipitate crystal structures in overaged Al-Mg-Si(-Cu) alloys, Mater. Charact. 160 (2020) 110087, http://dx.doi.org/10.1016/j.matchar.2019.110087.

[39] J.K. Sunde, S. Wenner, R. Holmestad, In situ heating TEM observations of evolving nanoscale Al–Mg–Si–Cu precipitates, J. Microsc. 279 (3) (2020) 143–147, http://dx.doi.org/10.1111/JMI.12845, https://onlinelibrary.wiley.com/doi/full/10.1111/jmi.12845 https://onlinelibrary.wiley.com/doi/abs/10.1111/jmi.12845 https://onlinelibrary.wiley.com/doi/10.1111/jmi.12845.

[40] E. Thronsen, C. Marioara, J. Sunde, K. Minakuchi, T. Katsumi, I. Erga, S. Andersen, J. Friis, K. Marthinsen, K. Matsuda, R. Holmestad, The effect of heavy deformation on the precipitation in an Al-1.3Cu-1.0Mg-0.4Si.wt.% alloy, Mater. Des. 186 (2020) http://dx.doi.org/10.1016/j.matdes.2019.108203.

[41] E. Thronsen, H. Mørkeseth, C.D. Marioara, K. Minakuchi, T. Katsumi, K. Marthinsen, K. Matsuda, R. Holmestad, The effect of small additions of fe and heavy deformation on the precipitation in an Al–1.1Mg–0.5Cu–0.3Si At. Pct alloy, Metall. Mater. Trans. A Phys. Metall. Mater. Sci. 53 (9) (2022) 3296–3310, http://dx.doi.org/10.1007/S11661-022-06744-9/FIGURES/8, URL: https://link.springer.com/article/10.1007/s11661-022-06744-9.

[42] R. Yuan, J. Zhang, L. He, J.M. Zuo, Training artificial neural networks for precision orientation and strain mapping using 4D electron diffraction datasets, Ultramicroscopy 231 (2021) 113256, http://dx.doi.org/10.1016/J.ULTRAMIC.2021.113256.

[43] S.C. Wang, M.J. Starink, Precipitates and intermetallic phases in precipitation hardening Al–Cu–Mg–(Li) based alloys, Int. Mater. Rev. 50 (4) (2005) 193–215, http://dx.doi.org/10.1179/174328005X14357, URL: https://www.tandfonline.com/doi/abs/10.1179/174328005X14357.

[44] P.N.H. Nakashima, The crystallography of aluminium and its alloys, in: G.E. Totten, M. Tiryakioğlu, O. Kessler (Eds.), Encyclopedia of Aluminum and Its Alloys, CRC Press, 2018, pp. 488–586.

[45] C. Dwyer, M. Weyland, L.Y. Chang, B.C. Muddle, Combined electron beam imaging and ab initio modeling of T1 precipitates in Al–Li–Cu alloys, Appl. Phys. Lett. 98 (20) (2011) 201909, http://dx.doi.org/10.1063/1.3590171, URL: https://aip.scitation.org/doi/abs/10.1063/1.3590171.

[46] J.M. Silcock, T.J. Heal, H.K. Hardy, Structural ageing characteristics of binary aluminium-copper alloys, J. Inst. Met. 82 (1953).

[47] B. Noble, G.E. Thompson, T 1 (Al2CuLi) precipitation in Aluminium–Copper–Lithium alloys, Metal Sci. J. 6 (1) (1972) 167–174, http://dx.doi.org/10.1179/030634572790445975, URL: https://www.tandfonline.com/doi/abs/10.1179/030634572790445975.

[48] J.S. Barnard, D.N. Johnstone, P.A. Midgley, High-resolution scanning precession electron diffraction: Alignment and spatial resolution, Ultramicroscopy 174 (2017) 79–88, http://dx.doi.org/10.1016/j.ultramic.2016.12.018.

[49] J.A. Mir, R. Clough, R. MacInnes, C. Gough, R. Plackett, I. Shipsey, H. Sawada, I. MacLaren, R. Ballabriga, D. Maneuski, V. O'Shea, D. McGrouther, A.I. Kirkland, Characterisation of the Medipix3 detector for 60 and 80 keV electrons, Ultramicroscopy 182 (2017) 44–53, http://dx.doi.org/10.1016/j.ultramic.2017.06.010.

[50] D.N. Johnstone, P. Crout, M. Nord, J. Laulainen, S. Høgås, EirikOpheim, B. Martineau, C. Francis, T. Bergh, E. Prestat, S. Smeets, andrew-ross1, S. Collins, I. Hjorth, Mohsen, T. Furnival, D. Jannis, N. Cautaerts, E. Jacobsen, AndrewHerzing, T. Poon, H.W. Ånes, J. Morzy, S. Huang, phillipcrout, T. Doherty, affaniqbal, T. Ostasevicius, mvonlany, R. Tovey, pyxem/pyxem: pyxem 0.13.3, Zenodo, 2021, http://dx.doi.org/10.5281/ZENODO.5075520, URL: https://zenodo.org/record/5075520.

[51] P. Crout, D.N. Johnstone, S. Høgås, B. Martineau, isabelwood100, J. Laulainen, H.W. Ånes, N. Cautaerts, S. Collins, S. Smeets, E. Jacobsen, J. Morzy, E. Prestat, phillipcrout, T. Doherty, AgBorrelli, T. Ostasevicius, R. Tovey, EirikOpheim, T. Bergh, pyxem/diffsims: diffsims 0.4.2, Zenodo, 2021, http://dx.doi.org/10.5281/ZENODO.4697299, URL: https://zenodo.org/record/4697299.

[52] C.J. Humphreys, The scattering of fast electrons by crystals, Rep. Progr. Phys. 42 (11) (1979) 1825, http://dx.doi.org/10.1088/0034-4885/42/11/002, https://iopscience.iop.org/article/10.1088/0034-4885/42/11/002 https://iopscience.iop.org/article/10.1088/0034-4885/42/11/002/meta.

[53] K. Momma, F. Izumi, VESTA 3 for three-dimensional visualization of crystal, volumetric and morphology data, J. Appl. Crystallogr. 44 (6) (2011) 1272–1276, http://dx.doi.org/10.1107/S0021889811038970, http://scripts.iucr.org/cgi-bin/paper?db5098 https://journals.iucr.org/j/issues/2011/06/00/db5098/.

[54] F. Pedregosa, G. Varoquaux, A. Gramfort, V. Michel, B. Thirion, O. Grisel, M. Blondel, P. Prettenhofer, R. Weiss, V. Dubourg, J. Vanderplas, A. Passos, D. Cournapeau, M. Brucher, M. Perrot, E. Duchesnay, Scikit-learn: Machine learning in {P}ython, J. Mach. Learn. Res. 12 (2011) 2825–2830.

[55] F.d.l. Peña, E. Prestat, V.T. Fauske, P. Burdet, T. Furnival, P. Jokubauskas, M. Nord, T. Ostasevicius, J. Lähnemann, K.E. MacArthur, D.N. Johnstone, M. Sarahan, J. Taillon, T. Aarholt, pquinn-dls, V. Migunov, A. Eljarrat, J. Caron, T. Poon, S. Mazzucco, B. Martineau, S. Somnath, T. Slater, C. Francis, actions-user, M. Walls, N. Tappy, N. Cautaerts, F. Winkler, G. Donval, Hyperspy/hyperspy: Release v1.6.4, 2021, http://dx.doi.org/10.5281/ZENODO.4923970, URL: https://zenodo.org/record/4923970.

[56] C. Boutsidis, E. Gallopoulos, SVD based initialization: A head start for nonnegative matrix factorization, Pattern Recognit. 41 (4) (2008) 1350–1362, http://dx.doi.org/10.1016/J.PATCOG.2007.09.010.

[57] H. Qiao, New SVD based initialization strategy for non-negative matrix factorization, Pattern Recognit. Lett. 63 (2015) 71–77, http://dx.doi.org/10.1016/J.PATREC.2015.05.019.

[58] O. Nicoletti, F. De La Peña, R.K. Leary, D.J. Holland, C. Ducati, P.A. Midgley, Three-dimensional imaging of localized surface plasmon resonances of metal nanoparticles, Nature 502 (7469) (2013) 80–84, http://dx.doi.org/10.1038/nature12469, URL: https://www.nature.com/articles/nature12469.

[59] E.F. Rauch, L. Dupuy, Rapid spot diffraction patterns idendification through template matching, Arch. Metall. Mater. 50 (1) (2005) 87–99, URL: https://www.infona.pl/resource/bwmeta1.element.baztech-article-BSW3-0014-0019.

[60] G. Carleo, I. Cirac, K. Cranmer, L. Daudet, M. Schuld, N. Tishby, L. Vogt-Maranto, L. Zdeborová, Machine learning and the physical sciences, Rev. Modern Phys. 91 (4) (2019) 045002, http://dx.doi.org/10.1103/RevModPhys.91.045002, URL: https://journals.aps.org/rmp/abstract/10.1103/RevModPhys.91.045002.

[61] Tensorflow Developers, TensorFlow, Zenodo, 2022, http://dx.doi.org/10.5281/ZENODO.6454633, URL: https://zenodo.org/record/6454633.

[62] J.K. Sunde, Ø. Paulsen, S. Wenner, R. Holmestad, Precipitate statistics in an Al-Mg-Si-Cu alloy from scanning precession electron diffraction data, in: Electron Microscopy and Analysis Group Conference 2017, Vol. 902, No. 1, EMAG2017, IOP Publishing, 2017, 012022, http://dx.doi.org/10.1088/1742-6596/902/1/012022, https://iopscience.iop.org/article/10.1088/1742-6596/902/1/012022 https://iopscience.iop.org/article/10.1088/1742-6596/902/1/012022/meta.

[63] T. Kavzoglu, Increasing the accuracy of neural network classification using refined training data, Environ. Model. Softw. 24 (7) (2009) 850–858, http://dx.doi.org/10.1016/J.ENVSOFT.2008.11.012.

[64] P. Crout, Methods and Applications for Nanometrology using Scanning Precession Electron Diffraction (Ph.D. thesis), University of Cambridge, 2022, http://dx.doi.org/10.17863/CAM.93907.

[65] E. Thronsen, T. Bergh, T.I. Thorsen, E.F. Christiansen, J. Frafjord, P. Crout, A.T.J.v. Helvoort, P.A. Midgley, R. Holmestad, Dataset for "Scanning precession electron diffraction data analysis approaches for phase mapping of precipitates in aluminium alloys", 2023, http://dx.doi.org/10.5281/zenodo.6645396.

[66] E. Thronsen, T. Bergh, T.I. Thorsen, E.F. Christiansen, J. Frafjord, SPED phase mapping, 2023, http://dx.doi.org/10.5281/zenodo.8321258.

[67] M. Själander, M. Jahre, G. Tufte, N. Reissmann, EPIC: An energy-efficient, high-performance GPU computing research infrastructure, 2019.